1.2-million-year band of Earth–Mars obliquity modulation on the evolution of cold late Miocene to warm early Pliocene climate

Jie Qin[1,2], Rui Zhang[1,2*], Vadim A. Kravchinsky[1,2, *], Jean-Pierre Valet[1,3], Leonardo Sagnotti[4], Jianxing Li[5], Yong Xu[6], Taslima Anwar[1,2], Leping Yue[1]

[1] Institute of Cenozoic Geology and Environment, State Key Laboratory of Continental Dynamics, Department of Geology, Northwest University, 710069 Xi'an, China

[2] Geophysics, Department of Physics, University of Alberta, T6G2E1 Edmonton, Canada

[3] Institut de Physique du Globe de Paris, 75238 Paris cedex 05, France

[4] Istituto Nazionale di Geofisica e Vulcanologia, 00143 Roma, Italy

[5] Chengdu Center of Geological Survey, Geological Survey of China, 610081 Chengdu, China

[6] Xi’an Center of Geological Survey, China Geological Survey, 710054 Xi’an, China

*** e-mails: ruizhang@nwu.edu.cn (R.Z.), vadim@ualberta.ca (V.A.K.)**

Abstract

The climatic transitions during the Miocene–Pliocene epochs had significant impacts on the worldwide biological diversity and were associated with large turnovers of continental vegetation and fauna. Previous studies have shown that late Miocene cooling and continental aridification which was initiated 7 Ma reversed to warm conditions across the Miocene–Pliocene Boundary ~ 5.3 Ma. Here we present detailed orbital pacing of Asian monsoon deposits to constrain further the global climate change during this period. We produce high-resolution magnetic susceptibility records which reveal that the 1.2 Myr obliquity modulation would have been the main driving factor of the cooling and warming that occurred ~ 7 Ma and 5.3 Ma, respectively. The Tibetan rise and closures of the Panama and Indonesian seaways enhanced the impact of the 405 kyr eccentricity cycles to an oscillatory climatic state while the Northern Hemisphere glaciations were increasing from 4 to 2.5 Ma.

astrochronology; Chinese Loess Plateau; grand obliquity modulation; magnetostratigraphy; Miocene-Pliocene; red clay

1. Introduction

In the late Miocene, terrestrial environments and ecosystems have undergone tremendous changes due to the presumed decline of atmospheric CO_2 between 8 and 6 Ma (Beerling et al., 2011; Bolton and stoll, 2013). This period has seen the replacement of large areas of tropical and subtropical forests by deserts (such as Sahara and Taklimakan Deserts) and the expansion of C4 grassland (Cerling et al., 1997; Schuster et al., 2006; Huang et al., 2007). The large restructuring of vegetation and landscape coincided with major turnovers in animal communities (Badgley et al., 2008). However, those continental environmental upheavals do not bring direct information on the temperature change during the Late Miocene (Herbert et al., 2016). The marine isotope record younger than the middle Miocene is characterized by periodic anomalies of the Antarctic ice volume that have been shown to be probably driven by obliquity in marine sequences from the peri-Antarctic margin (Naish et al., 2009). No clear trend suggests a long-term climatic change during the late Miocene (Zachos et al., 2001; Lewis et al., 2008; Westerhold et al., 2020). Recently, the integration of marine sea-surface temperature (SST) made it possible to estimate the evolution of global temperature during the Miocene (LaRiviere et al., 2012; Herbert et al., 2016). The late Miocene cooling did not lead monotonically to the ice age in the northern hemisphere that prevailed through most of the Pliocene (LaRiviere et al., 2012). Furthermore, temperature proxies indicate that cooling and aridification ceased during the Pliocene and that warmer conditions occurred after 5.3 Ma (Ravelo et al., 2004; Dowsett et al., 2005; Fedorov et al., 2006; Lawrence et al., 2006). Because the present-day global warming may induce Pliocene-like temperatures during the next decades, a good knowledge of the transition from a cold late-Miocene and warm early-middle Pliocene climate may provide a valuable analog for climatic projections (Burke et al., 2018).

It remains uncertain whether there is a link between contemporaneous atmospheric circulation, ecosystem changes in continental environments and the orbital variation effects recorded by climate proxies from the ocean realm. The hundreds of thousand-years' time scale low-latitude processes such as monsoon forcing on the upper-ocean circulation and its productivity strongly influences climate dynamics and constrains the reconstruction of ice volume and atmospheric greenhouse gas concentrations (Holbourn et al., 2018). The high topography of the Tibetan-Pamir Plateau contributes to amplify the Asian monsoon system that controls precipitation as well as the level of convection (An et al., 2001; Boos and Kuang, 2010). During the Quaternary, the climate was mostly affected by low-amplitude variability of precessional insolation modulated by the 405 and 100 kyr eccentricity cycles and the 41 kyr obliquity band (Nie et al., 2008; Hao et al., 2012; Nie, 2018; Sun et al., 2019). In earlier records from late Miocene to Pliocene, some may show unconventional cycles related to the orbital inclination rates of Earth and Saturn, called 173 kyr metronome for Asian monsoon, arouses our interest (Zhang et al., 2022). From analysis of the obliquity solution, both the 173 kyr and 1.2 Myr obliquity bands are of particular importance, the signal from the second is even much stronger than that of the first one (Laskar, 2020). In order to detect the longer orbitally forced cycle that has not been studied in the monsoon region, and to estimate whether it is associated with critical late Miocene-Pliocene climate transitions, we choose the eolian red clay deposits as the research subject.

2. Material and methods

2.1 Material

The monsoonal system is primarily characterized by intense summer rainfall over a wide area which lies along the continental-ocean pressure gradient and brings rainfall onto the continent (An et al., 2001; Sun et al., 2019). The East Asian monsoon (EAM) controls the amounts of precipitation and dust brought from the Indian to the Pacific Ocean by seasonal changes of warm moist air. Dry winds from the Asian high latitudes at high elevations transported dust that yielded the formation of the Chinese Loess Plateau (CLP) (Hao et al., 2012) (Figure 1a). The Liulin (LL) eolian red clay section (N37°21′, E110°45′) is flanked to the east by the Luliang Mountains and to the west by the Yellow River, dozens of kilometers away from the large mountain ridges (Figure 1b). The 68-meter thick wind-blown deposits consist of brownish red clay with sporadic and smaller caliche nodules (<5 cm) and abundant Fe–Mn coatings at the top intercalated by carbonate horizons. The bottom of the wind-blown deposits in the LL section was dated late Miocene by comparing the *Hipparion* teeth discovered at 56.3 m in the LL section with the analogous fossil layers in the neighbouring Fugu and Baode sections (Xue et al., 1995; Zhang et al., 1995; Zhu et al., 2008; Xu et al., 2013). This constraint enabled us to establish a first chronology of the LL section after correlating the magnetostratigraphic data to the geomagnetic polarity timescale (GPTS) (Ogg, 2012).

2.2 Methods

2.2.1 Sampling and Laboratory Measurements

30 samples at 2 m stratigraphic spacing were selected for thermomagnetic analyses using a MFK2 Kappabridge with a CS-4 furnace under an argon atmosphere to prevent oxidation during heating. Oriented paleomagnetic samples ~ every 10 cm and cut into 2 cm thick cubes for paleomagnetic measurements. A total of 618 samples were measured at 20 cm, increased to 10 cm in the parts where polarity reversals were more frequent. The samples were stepwise demagnetized every 50°C from room temperature up to 600°C using an MMTD 80 thermal demagnetizer. The natural remanent magnetization was measured using either a spinner JR6-A magnetometer or a 2G-755 magnetometer located in a low magnetic field space (<100 nT). The directions of the characteristic remanent magnetization were estimated by principal component analysis (Krischvink, 1980). Only determinations with maximum angular deviation (MAD) below 10° were accepted.

The magnetic susceptibility (MS) of powdered samples was measured using a Bartington MS-2 susceptibility meter. Grain size (GS) analysis was performed with a Mastersizer 2000 laser particle analyzer. 0.2 g powder samples were first treated with 10% H_2O_2 for about 15 min to remove organic matter and to ensure that the excess peroxide was destroyed. Carbonate was removed using 10% boiling HCl solution of 10ml and the samples were dispersed for 15 min. with 10 ml 10% $Na(PO_3)_6$ in an ultrasonic bath prior to the measurements.We performed a cyclostratigraphy analysis through spectral analysis of the MS and GS stratigraphic trends. We repeated the procedure to generate several new correlations between the magnetic polarity zones and the GPTS till the orbital periods were resolved clearly in the MS and GS stratigraphic trends.

2.2.2 Spectral Analysis

Spectral analysis was applied to check the occurrence of Milankovitch periodicities in MS and GS trends by attempting several correlations between each magnetic polarity pattern and the GPTS (Anwar et al., 2015; Zhang et al., 2021). Wavelet analysis with 95% confidence level of background red noise was used to calculate the spectra of the MS and GS records (Torrence and Compo, 1998). Before spectral analysis, we removed the long-term trends by subtracting a fitted smooth line in order to minimize the effects of non-orbital periods. We established an initial magnetostratigraphy and then generated several correlation patterns between each magnetic polarity pattern and the GPTS until the best orbital bands were clearly observed. After confirming the magnetochronology, both 405-kyr and 100-kyr cycles were extracted by filtering bands at the same time (with two bandwidths of 350–500 kyr and 80–125 kyr separately) in Matlab. Coherence between the band-pass filtered MS and eccentricity was scrutinized by calculating a correlation coefficient between the two-time series at zero phase using Matlab codes throughout the late Miocene – early and middle Pliocene. We shifted the MS curve towards younger or older ages) by ~ 30 to 200 kyr steps that were imposed by the coherency analysis in order to maximize the coherency between the two-time series with zero-time lag; then, a new time series could be obtained from the tuning process. The process was repeated many times until each peak of the two curves matched well and the correlation coefficient at zero-time lag reached the maximum. Midway in the process, for a very small time lag between the two series, we stretched or squeezed the MS curve manually to make it match the eccentricity. Each tuned timescale was also applied to GS records at the same time. The spectral powers were produced to help determine our final age model.

3. Results

3.1 Rock magnetism and magnetostratigraphy

The plots of MS (χ) versus temperature (T) show that the heating and cooling cycles are nearly reversible (Figure 2). The sharp drop of χ between ~400–585 °C, indicates the presence of magnetite. Further decrease of χ to 700 °C reveals that hematite is also present. Representative demagnetization results for different depths are shown in Figure 3 with orthogonal vector diagrams. Our demagnetization results demonstrated that the low-temperature overprints generally ranged from the room temperature to 200 °C. After the elimination of the low-temperature component, the samples yielded a stable characteristic remanent magnetization (ChRM) tending to the origin.

Paleomagnetic analysis reveals five normal (N1 – N5) and five reversed (R1 – R5) polarity intervals from the reliable ChRM directions (Figure 4). All magnetostratigraphic intervals are established based on more than 4 coinciding samples (and over at least 0.8 meters in the depth) to excluded the effects from small amplitude and short period anomalies (Zhang et al., 2018; Zhang, Kravchinsky, et al., 2021, Zhang, Wei, et al., 2021 Zhang et al., 2022). Three brief normal polarity events (less than or equal to 4 coinciding samples and less than 0.8 m in thickness) were also verified from the ChRM recording (red horizons in Figure 3). Sand, gravel and mammalian fossils found in the lower part of the section show negligible significant influence from alluvial processes (Figure 4a). The dense carbonate layers and mud-stone suggest that during the ongoing uplift of the Lvliang Mountains, groundwater was of interest from time to time because it could re-magnetize large amounts of wind-blown sediments. We marked five such prominent layers with light green shading in Figure 4.

The fossils found from sandy layers at 56.3 m in depth of the section containing the *Hipparion* fauna were dated between 7.2 and 6.8 Ma at adjacent Fuxing section, 7.0–6.7 Ma at the Wujiamao and Baode sections (Zhu et al., 2008; Xu et al., 2013; Zhang et al., 2022). Here, *Hipparion* teeth are thought to be ~ 6.8 Ma in the magnetostratigraphy when N5 and R5 are correlated to C3An and C3Br. This constraint enabled us to establish a first chronology after correlating the magnetostratigraphic data to the geomagnetic polarity timescale (GPTS) (Ogg, 2012). Following the visual correlation, N1 – N3 are associated with C3n.1n – C3n.3n while a brief normal event remains a question mark with respect to C3n.4n. In the field observation, dense calcareous nodules, mudstone and carbonate layers developed from 18 – 27 m, which means underneath the short polarity record at ~18 m, records of rising groundwater flows had been continuously superimposed in the stratum from 27 m and above. Such rework could have disrupted the original paleomagnetism, causing the remagnetization to obscure the previous record. The lower two events at ~ 60 m from the section are only recorded in the sandy layer. As paleomagnetic samples in sand are likely acquired viscous magnetic fields through remagnetization, further verification of the authenticity is required for these question marked red horizons (Zhang et al., 2018; Zhang, Kravchinsky et al., 2021; Zhang, Wei, et al., 2021; Zhang et al., 2022). Considering that there are dense carbonate and sandy layers at the depth of 41-46 m, it indicates that groundwater might also affect the remnant magnetization of the N4 polarity zone. In this case, only N1, N2, N3 and N5 can be used for the initial targeting age prior to tuning to the orbital parameters. Then, we performed a cyclostratigraphy analysis through spectral analysis of the MS and GS records. To verify the correctness of our magnetostratigraphic correlation we generated several new correlations between the magnetic polarity zones and the GPTS and performed spectral analysis until the orbital periods were clearly resolved in the MS and GS records. Clear peaks of the 405 kyr eccentricity band can be observed between 7 and 5.4 Ma (Figure. 5A and 5C). The 100 kyr cycles can also be identified at around 6.2–6 Ma in the MS spectrum even though their power amplitudes were much weaker than the 405 kyr power (Figure 5A). Analogously, a relatively low-amplitude 100 kyr cycles revealed between 5.9 and 5.7 Ma in the GS spectrum (Figure 5C). The final magnetostratigraphic correlation that incorporated the cyclostratigraphic procedure described in Methods is shown in Figure 4.

3.2 Orbital tuning and astronomical calibration

Once the magnetostratigraphic age of the LL section has been compatible with the cyclostratigraphy, we conducted two-channel-band filtering (405 kyr and 100 kyr) for both MS and GS data to highlight the visuality of the eccentricity band and tunes the filtered record cycle-by-cycle to the long eccentricity maxima (405 kyr) and short eccentricity maxima (100 kyr) at the same time (Figure 5). To examine the coupling between our records and eccentricity cycles, we calculated the correlation coefficient between filtered MS and eccentricity at zero phase. Then we shifted the filtered MS curve to the left or right at a short time span implied by the coherency analysis in order to fit it with the filtered eccentricity 405 kyr until the correlation coefficient was maximized. After that we carried out fine adjustments to the stronger 100 kyr cycle improving further the correlation coefficient. We repeated this procedure until the curve matching and correlation coefficients were maximized. During the tuning processes, we also adjusted some small time lags between the two series, by stretching or squeezing the MS peaks to the eccentricity peaks (Figure 5B). The final astronomical calibration based on the MS turning was applied to the GS record (Figure 5D).

The calculated sedimentation rate (Figure 6) varied from 1.6 to 3.6 cm/kyr with an average of 2.2 cm/kyr. These values are typical of the eolian red clay dust in the CLP (e.g. Nie et al., 2008; Anwar et al., 2015; Zhang et al., 2018).

3.3 Stratigraphic correlations

To investigate large-scale climate variations we first compare the LL section to the classical Jingchuan section (JC) which is located in the middle of CLP (Ding et al., 2001), and the adjacent Shilou (SL) section which is situated close to LL and stratigraphically continues LL to the younger age until 2.6 Ma (Ding et al., 2001; Anwar et al., 2015) (Figure 7). Further Comparsions to the eastern and western edges of CLP can be found in Supplementary Fig. 1.

The bottom age of the SL section was extensively debated and assigned from the late Miocene at 11 Ma (Xu et al., 2009, 2012), 8 Ma (Ao et al., 2016; 2018), to the early Pliocene at 5.2 Ma (Anwar et al., 2015; Zhang, et al., 2018, 2022). Both Xu et al. (2012) and Ao et al. (2016, 2018) mistakenly assigned the finding of micromammal *Meriones* sp. at a depth of 46.6 m in the SL section to correspond to the Miocene age. However, the original studies of Zheng et al. (2000, 2001) cited by Ao et al. (2016, 2018) did not confirm that the *Meriones* sp. belonged to the Miocene. Zheng et al., (2000, 2001) established that another micromammal *Pseudomeriones* sp. existed in the Miocene, whereas *Meriones* sp. lived during the Pliocene and Pleistocene (Dianat et al., 2017). Therefore the chronology presented in Anwar et al. (2015) and Zhang et al. (2018, 2022) is consistent with the Pliocene-Pleistocene age for the SL section. We note that the bottom of the SL red clay is not exposed in the outcrop and in the future it is possible to reach the late Miocene red clay layers using drilling. The LL section is older than the SL section considering the fossil evidence from both SL and LL that is supported by the magnetostratigraphy.

The LL section is located in a valley with a lower elevation compared to the SL section and has ~ 400 m height difference with 40 km horizontal separation of the sections

(Figure 1b). Taking it into account we combined both records that have overlap between each other into a long magnetic susceptibility (LMS) record spanning from the Gauss chron to C3A chron (Figure 7). Both MS records were stacked together by averaging the values between two parts in the overlapping interval of 5.2 – 4 Ma. Figure 7 demonstrates similarities of the general long-term trends between LMS and the JC section MS record (Ding et al., 2001), while smaller scale features differ in the terms of amplitudes.

4. Discussion

4.1 Discovery of the 1.2 Myr cycle in the Asian monsoon record

The typical changes of MS records in the eolian sediments of CLP are well known for their close match with the global ice-interglacial cycles depicted by the $\delta^{18}O$ records in marine sediments and by the time-series of summer insolation at 65^{o} N derived from orbital solutions (Laskar et al., 2004). We obtained independent climate records from terrestrial archives of CLP in order to reconstruct the atmospheric circulation in eastern Asia since the late Miocene. We compared our stacked LMS record from the eastern part of CLP with the inland JC red clay section (Figure 7a-d) (Ding et al., 2001).

The results of the wavelet analysis of the LMS record show a clear 405 kyr eccentricity cycle between 7 and 2.5 Ma (Figure 7e) which is linked to the gravitational interaction of Jupiter and Venus (g2–g5), while the MS in the central CLP indicates an accentuation of the 405 kyr band between 4 and 2.5 Ma (Figure 7f). Interestingly, a ~1.2 Myr grand cycle of s4 – s3 obliquity modulation, linked to the orbital inclination rates of Mars and Earth, is superimposed with the 405 and 100 kyr bands (Figure 7e & 7f) similarly to previous climatic records (van Dam et al., 2006) and is interpreted as beats between secular frequencies p+s4 and p+s3 (Laskar et al., 2004). The chaotic solar system has two major secular resonances. The first argument, $\theta = (s4 - s3) - 2\,(g4 - g3)$ draws particular attention because the two longest orbital secular frequencies, obliquity and precession modulations, from s4 – s3 and g4 – g3 (~2.4 Myr) experienced intermittent chaotic transitions at ~ 2:1 resonance states, when ~1.2 Myr cycle dominates since 50 Ma (Hinnov, 2000; Laskar et al., 2004; Palike et al., 2004; Crampton et al., 2018).

To further highlight the expression of the 405 and 100 kyr eccentricity bands within the LMS and JS records, we applied a two-channel band-pass filter with 350–500 kyr and 80–125 kyr bandwidths, respectively (red curves in Figure 8) after removing the long-term trend that could be related to tectonic processes in the region (Anwar et al., 2015; R. Zhang, Kravchinsky, et al., 2021; Zhang et al., 2022). The minima of each 405 kyr cycle after the filter application between ~5.3 Ma and 2.5 Ma for both MS curves (Figure 8d & 8e) correlate with the eccentricity maxima (Figure 8c). However, prior to this period the curves are out of phase suggesting that some other signal should have affected the climate variations during the late Miocene. In contrast to the filtered signals and astronomical cycles (red solid and green dashed lines), the unfiltered MS (Fig. 8d, f) curves show less variability but the conspicuous grand cycle related to the 1.2 Myr obliquity modulation is evident between 7.1 and 4 Ma.

4.2 Global documentation of the 1.2 Myr cycle that drives the Miocene-Pliocene climate variations

Obliquity, precession and their modulations have been shown to be important driving forces of the global monsoon system which is sensitive to change in insolation, waxing and waning of ice sheets and CO_2 concentration (Prell and Kutzbach, 1992; Nie et al., 2008; Anwar et al., 2015; Nie, 2018; Zhang et al., 2022). Various time series, such as MS, $\delta^{18}O$, SST and atmospheric CO_2 levels, display a significant climatic transition at ~5.3 Ma (Beerling et al., 2011; Herbert et al., 2016; Holbounr et al., 2018; Tian et al., 2008; Liu et al., 2019) (Fig. 9). The MS records show that the intensification of the Tibetan Plateau rise enhanced the 405 kyr band by a strengthened summer monsoon since ~ 3.6 – 4.2 Ma (Fig. 9b, c) (Nie et al., 2008). Therefore, we suggest that tectonic processes that impacted regional land-sea heat exchanges influenced strongly the orbital-sensitive climate fluctuations, which, in turn, induced significant changes in the insolation-forced summer monsoon and led to introducing the tectonic related long-term trend towards two-three times higher values of MS in the interval between ~ 4.2 and 3.6 Ma (Fig. 9b, c). In the ocean, the negative shifts of benthic $\delta^{18}O$ records (Fig.9d) correspond to the increase of MS (Fig.9b, c) that is consistent with a dominant summer monsoon regime linked to a global warming at 5.3 Ma (Holbourn et al., 2018). In contrast, the positive shifts of $\delta^{18}O$ (Fig. 9d) and the decrease of MS (Fig. 9b, c) and SST (Fig. 9h) correspond to a global cooling and inland aridification that led to the birth of the Sahara and Taklimakan deserts ~ 7 Ma (Schuster et al., 2006; Sun et al., 2009).

Previous studies have pointed out that a strengthened winter monsoon during the 7.1–5.5 Ma time interval was associated with an expansion of ice sheets in the Northern Hemisphere (Wolf-Welling et al., 1996; Thiede et al., 1998; Holbourn et al; 2018) and indicated a global cooling during the late Miocene (Zachos et al., 2001). The $\delta^{18}O$ record of benthic foraminifera showed a clear decrease indicating a warming transition ~5.5 – 5.3 Ma. (Holbourn et al; 2018; Westerhold et al., 2020). A stronger deep-sea ventilation could have constrained warmer and saline surface water to flow up to the high-latitude North Pacific and Atlantic subtropical gyres and thus deliver additional heat and moisture to the Northern Hemisphere that contributed to a global warming 5.3 Ma. Such interpretation of both climatic variations at ~7 and 5.3 Ma is supported by the variability of the 1.2 Ma obliquity modulation (Fig. 9a & Fig. 10) during the 7.6 – 3.6 Ma intervals. The grand obliquity curve is on the descent at 7 Ma and on the rise at 5.3 Ma.

Several lines of evidence indicate that the closure of the Panama and Indonesia seaways may have also caused a significant reorganization of ocean circulation and increased the Gulf Stream yielding substantial transfer of warm and saline water masses to high northern latitudes during the Miocene-Pliocene between 6 and 2.7 Ma (Cane et al., 2001; Haug et al., 2001; Molnar, 2008). The warm conditions at high latitudes (Fig. 9f) may result from the massive input of warmer water. The planktonic foraminifera isotopic records from the Caribbean Sea indicate that salinity of the Caribbean surface waters already started to increase at the beginning of Pliocene, suggesting a weakened surface water circulation between the tropical Atlantic and Pacific Oceans as a result of the growth of the Central American isthmus of Panama (Haug et al., 1998). It probably led to a climate pattern of a 405-kyr cycle in the western Hemisphere even earlier than the

Asian Monsoon region (Fig. 9g) (Nie, 2018). However, there is still controversy, to determine when the seaway closed, if not possible, until the "Great American Exchange" of Vertebrates between North and South America that occurred ~ 2.7 – 2.6 Ma (Molnar, 2008). On the other hand, the thickening of the equatorial Western Pacific warm pool triggered by the closure of the Panama and Indonesian seaways may have expanded the exchanges of heat and moisture toward high latitudes. This process contributed to warming up of the South China Sea water and to increasing the precipitation on the Asian continent (Yan et al., 1992; Li et al., 2008). The gradual growth of the Tibetan Plateau ~ 4.2 Ma may have also increased the air pressure gradient between land and sea, resulting in greater seasonal precipitation within the monsoon influence region. The 1.2 and 0.405 Myr long amplitude modulations of the obliquity and precession cycles are prominent features of the climate pattern between the late Miocene and Pliocene, especially for the Asian monsoon.

5. Conclusions

Our interpretation of the LMS record shows that the Asian summer monsoon appears to be orbitally controlled by the 1.2 Myr grand obliquity cycle band between 7.7 and 4 Ma and by the 0.405 Myr long eccentricity band between 4 and 2.5 Ma. We conclude that global cooling and warming that occurred 7 and 5.3 Ma respectively, as well as the Antarctic ice volume, carbon cycle dynamics and the monsoon forcing of the upper-ocean circulation were all triggered by the grand obliquity variations before the middle Pliocene. Since then, a series of major tectonic events such as the closure of the Panama and Indonesian seaways and the uplift of the Tibetan Plateau, accelerated the transition from a 1.2 Myr obliquity-dominated to a 0.405 Myr eccentricity-dominated climate variability for the Asian monsoon.

Acknowledgments

This study was funded by the National Natural Science Foundation of China (41772027, 41972035 and 41950410574) for R.Z., J.Q. and J.L., the China Scholarship Council for J.Q., and the Natural Sciences and Engineering Research Council of Canada (NSERC grant RGPIN-2019-04780) for V.A.K. The data related to the manuscript will be available at https://zenodo.org after the manuscript is accepted for publication. We temporarily upload the data to the supplementary file for review.

Competing Interests

The authors declare no competing interests.

References

An, Z., Kutzbach, J.E., Prell, W.L., Porter, S.C., 2001. Evolution of Asian monsoons and phased uplift of the Himalaya–Tibetan plateau since Late Miocene times. *nature* 411, 62–66.

Anwar, T., Kravchinsky, V.A., Zhang, R., 2015. Magneto-and cyclostratigraphy in the red clay sequence: New age model and paleoclimatic implication for the eastern Chinese Loess Plateau. *Journal of Geophysical Research: Solid Earth*, 120, 6758–6770.

Ao, H., Roberts, A.P., Dekkers, M.J., Liu, X., Rohling, E.J., Shi, Z., An, Z., Zhao, X., 2016. Late Miocene–Pliocene Asian monsoon intensification linked to Antarctic ice-sheet growth. Earth and Planetary Science Letters 444, 75–87.

Badgley, C., Barry, J.C., Morgan, M.E., Nelson, S.V., Behrensmeyer, A.K., Cerling, T.E., Pilbeam, D., 2008. Ecological changes in Miocene mammalian record show impact of prolonged climatic forcing. *Proceedings of the National Academy of Sciences*, *105*, 12145–12149.

Beerling, D.J., Royer, D.L., 2011. Convergent Cenozoic CO_2 history. *Nature Geoscience* 4, 418–420.

Bolton, C.T., Stoll, H.M., 2013. Late Miocene threshold response of marine algae to carbon dioxide limitation. *Nature* 500, 558–562.

Boos, W.R., Kuang, Z., 2010. Dominant control of the South Asian monsoon by orographic insulation versus plateau heating. *Nature* 463, 218–222.

Burke, K.D., Williams, J.W., Chandler, M.A., Haywood, A.M., Lunt, D.J., Otto-Bliesner, B.L., 2018. Pliocene and Eocene provide best analogs for near-future climates. *Proceedings of the National Academy of Sciences*, 115, 13288–13293.

Cane, M.A., Molnar, P., 2001. Closing of the Indonesian seaway as a precursor to east African aridification around 3–4 million years ago. *Nature* 411, 157–162.

Cerling, T.E., Harris, J.M., MacFadden, B.J., Leakey, M.G., Quade, J., Eisenmann, V., Ehleringer, J.R., 1997. Global vegetation change through the Miocene/Pliocene boundary. *Nature 389*, 153–158.

Crampton, J.S., Meyers, S.R., Cooper, R.A., Sadler, P.M., Foote, M., Harte, D., 2018. Pacing of Paleozoic macroevolutionary rates by Milankovitch grand cycles. *Proceedings of the National Academy of Sciences* 115, 5686–5691.

Dianat, M., Darvish, J., Cornette, R., Aliabadian, M., Niolas, V., 2017. Evolutionary history of the Persian Jird, *Meriones persicus*, based on genetics, species distribution modelling and morphometric data. Journal of Zoological Systematics & Evolutionary Research, 55, 29–45.

Ding, Z., Yang, S., Hou, S., Wang, X., Chen, Z., Liu, T., 2001. Magnetostratigraphy and sedimentology of the Jingchuan red clay section and correlation of the Tertiary eolian red clay sediments of the Chinese Loess Plateau. *Journal of Geophysical Research: Solid Earth*, 106, 6399–6407.

Dowsett, H.J., Chandler, M.A., Cronin, T.M. and Dwyer, G.S. Middle Pliocene sea surface temperature variability. Paleoceanography, 20, PA2014 (2005).

Fedorov, A.V., Dekens, P.S., McCarthy, M., Ravelo, A.C., deMenocal, P.B., Barreiro, M., Pacanowski, R.C., Philander, S.G., 2006. The Pliocene Paradox (Mechanisms for a Permanent El Nino). *Science* 312, 1485–1489.

Hao, Q., Wang, L., Oldfield, F., Peng, S., Qin, L., Song, Y., Xu, B., Qiao, Y., Bloemendal, J., Guo, Z., 2012. Delayed build-up of Arctic ice sheets during 400,000-year minima in insolation variability. *Nature* 490, 393–396.

Haug, G.H., Tiedemann, R., 1998. Effect of the formation of the Isthmus of Panama on Atlantic Ocean thermohaline circulation. *Nature* 393, 673–676.

Haug, G.H., Tiedemann, R., Zahn, R., Ravelo, A.C., 2001. Role of Panama uplift on oceanic freshwater balance. Geology, 29, 207–210.

Herbert, T.D., Lawrence, K.T., Tzanova, A., Peterson, L.C., Caballero-Gill, R., Kelly, C.S., 2016. Late Miocene global cooling and the rise of modern ecosystems. *Nature Geoscience* 9, 843–847.

Hinnov, L.A., 2000. New perspectives on orbitally forced stratigraphy. *Annual Review of Earth and Planetary Sciences 28*, 419–475.

Holbourn, A.E., Kuhnt, W., Clemens, S.C., Kochhann, K.G., Jöhnck, J., Lübbers, J., Andersen, N., 2018. Late Miocene climate cooling and intensification of southeast Asian winter monsoon. *Nature Communications* 9, 1584.

Huang, Y., Clemens, S.C., Liu, W., Wang, Y., Prell, W.L., 2007. Large-scale hydrological change drove the late Miocene C4 plant expansion in the Himalayan foreland and Arabian Peninsula. *Geology* 35, 531–534.

LaRiviere, J.P., Ravelo, A.C., Crimmins, A., Dekens, P.S., Ford, H.L., Lyle, M., Wara, M.W., 2012. Late Miocene decoupling of oceanic warmth and atmospheric carbon dioxide forcing. *Nature* 486, 97–100.

Laskar, J., Correia, A.C.M., Gastineau, M., Joutel, F., Levrard, B., Robutel, P., 2004. Long term evolution and chaotic diffusion of the insolation quantities of Mars. *Icarus, 170*, 343–364.

Laskar, J., Joutel, F., Boudin, F., 1993. Orbital, precessional, and insolation quantities for the Earth from -20 Myr to +10 Myr. *Astronomy and Astrophysics*, 270, 522–533.

Lawrence, K.T., Liu, Z., Herbert, T.D., 2006. Evolution of the Eastern Tropical Pacific Through Plio-Pleistocene Glaciation. *Science* 312, 79–83.

Lewis, A.R., Marchant, D.R., Ashworth, A.C., Hedenäs, L., Hemming, S.R., Johnson, J.V., Leng, M.J., Machlus, M.L., Newton, A.E., Raine, J.I., Willenbring, J.K., 2008. Mid-Miocene cooling and the extinction of tundra in continental Antarctica. *Proceedings of the National Academy of Sciences 105*, 10676–10680.

Li, F., Rousseau, D.D., Wu, N., Hao, Q., Pei, Y., 2008. Late Neogene evolution of the East Asian monsoon revealed by terrestrial mollusk record in Western Chinese Loess Plateau: from winter to summer dominated sub-regime. *Earth Planet. Sci. Lett.* 274, 439–447.

Liu, J., Tian, J., Liu, Z., Herbert, T.D., Fedorov, A.V., Lyle, M., 2019. Eastern equatorial Pacific cold tongue evolution since the late Miocene linked to extratropical climate. Science advances 5, eaau6060.

Molnar, P., 2008. Closing of the Central American Seaway and the Ice Age: A critical review. Paleoceanography, 23, PA2201, doi: 10.1029/2007PA001574.

Naish, T., Powell, R., Levy, R., Wilson, G., Scherer, R., Talarico, F., Krissek, L., Niessen, F., Pompilio, M., Wilson, T., Carter, L., 2009. Obliquity-paced Pliocene West Antarctic ice sheet oscillations. *Nature* 458, 322–329.

Nie, J., King, J.W., Fang, X., 2008. Tibetan uplift intensified the 400 ky signal in paleoclimate records at 4 Ma. Geological Society of America Bulletin 120, 1338–1344.

Nie, J. 2018. The Plio-Pleistocene 405-kyr climate cycles. Palaeogegraphy, palaeoclimatology, palaeoecology 510, 26–30.

Ogg, J. G., 2012. Geomagnetic Polarity Time Scale. In F. M. Gradstein, J. G. Ogg, M. D. Schmitz, & G. M. Ogg (Eds.), The Geologic Time Scale 2012. Amsterdam: Elsevier, (pp. 85–113).

Prell, W.L., Kutzbach, J.E, 1992. Sensitivity of the Indian monsoon to forcing parameters and implications for its evolution. *Nature* 360, 647–652.

Ravelo, A.C., Andreasen, D.H., Lyle, M., Lyle, A.O., Wara, M.W., 2004. Regional climate shifts caused by gradual global cooling in the Pliocene epoch. *Nature* 429, 263–267.

Schuster, M., Duringer, P., Ghienne, J.F., Vignaud, P., Mackaye, H.T., Likius, A., 2006. Brunet, M. The age of the Sahara Desert. Science 311, 821.

Sun, J., Zhang, Z., Zhang, L., 2009. New evidence on the age of the Taklimakan Desert. *Geology 37*, 159–162.

Sun, Y., Yin, Q., Crucifix, M., Clemens, S.C., Araya-Melo, P., Liu, W., Qiang, X., Liu, Q., Zhao, H., Liang, L., Chen, H., 2019. Diverse manifestations of the mid-Pleistocene climate transition. *Nature communications*, *10*, 352.

Thiede, J., Winkler, A., Wolf-Welling, T., Eldholm, O., Myhre, A.M., Baumann, K.H., Henrich, R., Stein, R., 1998. Late Cenozoic history of the Polar North Atlantic: results from ocean drilling. Quaternary Science Reviews, 17, 185–208.

van Dam, J., Abdul Aziz, H., Alvarez Sierra, M.A., Hilgen, F.J., van den Hoek Ostende L.W., Lourens, L.J., Mein, P., van der Meulen, A.J., Pelaez-Campomanes, P. , 2006. Long-period astronomical forcing of mammal turnover. *Nature* 443, 687–691.

Westerhold, T., Marwan, N., Drury, A.J., Liebrand, D., Agnini, C., Anagnostou, E., Barnet, J.S., Bohaty, S.M., De Vleeschouwer, D., Florindo, F., Frederichs, T., 2020. An astronomically dated record of Earth’s climate and its predictability over the last 66 million years. Science, 369, 1383–1387.

Wolf-Welling, T.C., Cremer, M., O'Connell, S., Winkler, A., Thiede, J., 1996. Cenozoic Arctic gateway paleoclimate variability: Indications from changes in coarse-fraction composition. Proceedings of the Ocean Drilling Program, Scientific Results 151, 515–568.

Xu, Y., Yue, L., Li, J., Sun, L., Sun, B., Zhang, J., Ma, J., Wang, J., 2009. An 11-Ma-old red clay sequence on the Eastern Chinese Loess Plateau. Palaeogeography, Palaeoclimatology, Palaeoecology 284, 383–391.

Xu, Y., Yue, L., Li, J., Wang, J., Sun, B., Sun, L., Zhang, J., Ma, J., 2013. Late Neogene red clay in the Fuxing area of western foothills of the Luliang Mountain. Journal of Stratigraphy, 37, 33–40 (in Chinese).

Yan, X., Ho, C., Zheng, Q. and Klemas, V., 1992. Temperature and size variabilities of the west Pacifific warm pool. *Science* 258, 1643–1645.

Zachos, J., Pagani, M., Sloan, L., Thomas, E., Billups, K., 2001. Trends, rhythms, and aberrations in global climate 65 Ma to present. science 292, 686–693.

Zheng, S., Zhang, Z., 2000. Late Miocene-Early Pleistocene micromammals from Wenwanggou of Lingtai, Gansu, China. *Vertebrata PalAsiatica*, *38*, 58–71.

Zheng, S., Zhang, Z., 2001. Late Micene-early Pleistocene biogeography of the Leijiahe area, Lingtai, Gansu. Vertebrata PalAsiatica 39, 215–228 (in Chinese).

Zhang, R., Kravchinsky, V. A., Anwar, T., Yue, L., Li, J., Jiao, J., 2018. Comment on "Late Miocene-Pliocene Asian monsoon intensification linked to Antarctic ice-sheet growth" [Earth Planet. Sci. Lett. 444 (2016) 75-87]. Earth and Planetary Science Letters 503, 248–251.

Zhang, R., Kravchinsky, V. A., Qin, J., Goguitchaichvili, A., Li, J., 2021. One and a Half Million Yearlong Aridity During the Middle Eocene in North-West China Linked to a Global Coooling Episode. *Journal of Geophysical Research: Solid Earth 126*, e2020JB021037.

Zhang, R., Wei, X., Kravchinsky, V. A., Yue, L., Zheng, Y., Qin, J., Yang, L., Ma, M., Xian, F., Gong, H., Zhang, Y., Liu, X., 2021. “Tiny wiggles” in the late Miocene red clay deposits in the north-east of the Tibetan Plateau. Geophysical Research Letters, 48, e2021GL093962.

Zhang, R., Li, X., Xu, Y., Li, J., Sun, L., Yue, L., Pan, F., Xian, F., Wei, X., Cao, Y., 2022. The 173-kyr obliquity cycle pacing the Asian monsoon in the eastern Chinese Loess Plateau from late Miocene to Pliocene. Geophysical Research Letters, 49, e2021GL097008.

Figure Captions

Figure 1. (a) Topographic map of the present-day Chinese Loess Plateau with studied locations (yellow star and yellow dots). Liulin (yellow star); SL- Shilou, JC- Jingchuan. (b) Map showing the location of LL (green triangle) and SL (red star) red clay sections and the surrounding main rivers. Red dashed lines represent the contours and the elevation is in meters.

Figure 2. χ-T curves for selected samples from the Liulin red clay sequence. The red and blue lines represent heating and cooling curves, respectively.

Figure 3. Representative thermal demagnetization curves for different depths.

Figure 4. Lithostratigraphy, inclination, declination and VGP as a function of depth, and the magnetic polarity interpretation of the Liulin red clay section, together with a correlation to the geomagnetic timescale (Ogg, 2012). Red dots show the measuring samples. Legend: 1—red clay with strong pedogenesis, 2—sandy red clay, 3—red clay with weak pedogenesis, 4—carbonate layer, 5—mudstone, 6—fossil, 7—sandstone, 8—gravel, 9—carbonate nodules.

Figure 5. Wavelet analysis of the magnetic susceptibility signal before (a) and after

tuning (b), the coarse fraction (>63μm) content before (c) and after tuning (d). Magnetic susceptibility and Grain size was detrended with the Lowess smoothing method. The red line is the two-band-filter signal with bandwidths of 350–500 kyr and 80–125 kyr. The green solid line shows the long trend of MS (a,b)and GS (c,d) signals. The purple dashed line marks the orbital period. The thin black contour encloses regions of greater than 95% confidence for a red-noise process with a lag coefficient of 0.8. The thick black contour indicates the cone of influence. The global wavelet spectrum to the right illustrates the mean red noise spectrum, as indicated by the green dashed line. The color bars correspond to wavelet power.

Figure 6. Sedimentation rates are determined on the basis of the magnetostratigraphic correlations. Black dashed lines denote the typical sedimentation rate range for the red clay of the CLP (Zhang et al., 2018). The red dashed line represents the average sedimentation rate of the Liulin section determined by the magnetostratigraphy.

Figure 7. Comparison of magnetic susceptibility as a function of age from red clay sections in the Chinese Loess Plateau. Three stages of different climate conditions as shown by the MS. (a) MS of the LL red clay section. (b) MS of the SL red clay section (Anwar et al., 2015). (c) LMS of the combined LL and SL red clay sections. (d) MS of the JC red clay section (Ding et al., 2001). (e)Wavelet analysis of magnetic susceptibility records from the LMS. (f) Wavelet spectrum of magnetic susceptibility from the JC section.

Figure 8. Milankovitch cycles between 7.8 and 2.5 Ma derived from the astronomical solution (Laskar et al., 2004) and the Asian monsoon record. a. Amplitude modulation of the precession solution (blue line) with its envelope curve (black dashed line) with the ~100,000 and ~405,000 cycles. b. Amplitude modulation (green line) of the obliquity solution (Laskar et al., 2004) (blue line). c. Eccentricity solution. d. Long magnetic susceptibility (LMS) detrended by the Lowess smoothing method (blue). f. Magnetic susceptibility from JC section after detrending using the Lowess smoothing method (blue) (Ding et al., 2001). Red lines indicate the two-band filter with bandwidths of 350–500 kyr and 80–125 kyr in d,e,f,g,h. Green dashed curves show the ~1.2 Myr obliquity modulations coupling with MS results (d,e).

Fig. 9. Compilation of Asian monsoon and global climatic proxies. a. Illustration of the eccentricity solution (Laskar et al., 2004) (blue solid and dashed lines) and the ~1.2 Myr grand cycles/obliquity modulations (green dashed line). b. Combined LMS record of the LL and SL sections. c. MS from JC section in the central CLP (Ding et al., 2001). d. Benthic δ18O global record (Westerhold et al., 2020) (blue) and benthic δ18O record from ODP Site 1148 (Tian et al., 2008) (orange). e. Stacked SST from mid-high (pink) and tropical (brown) latitudes. Pacific mid-high latitude records are integrated from DSDP Site 594, ODP Sites 883/884, 887, 1010, 1012,1021, 1125 and 1208; Pacific tropical records are integrated from the IODP Sites U1337, U1338, ODP Sites 846, 847, 850 and 1241 (Liu et al., 2019). f. Atmospheric CO2 history during the past 8 Myr from

different proxies (Beerling et al., 2011; Herbert et al., 2016). Horizontal red line indicates the Northern Hemisphere glaciation threshold (approx. 280 ppm). g. δ13C record (yellow) and carbonate sand-fraction mass accumulation rates (purple) from ODP site 999 (Haug et al., 1998).

Fig. 10. The simplified climate mode for Asian monsoon from late Miocene to Pliocene. a. Eccentricity solution (Laskar et al., 2004) (blue solid and dashed lines), obliquity solution (Laskar et al., 2004) (red line), and the ~1.2 Myr grand cycles (green solid line from 8 to 4 Ma and green dashed line from 4 to 2.5 Ma). b. Mathematical model showing the 1.2 Myr grand cycles (red) during the 8 to 4 Ma ($Y1 = \cos(2\times\pi\times(1/1200)\times t)$); the 400 eccentricity cycles (blue) ($Y2 = \sin(2\times\pi\times(1/400)\times t)$ and the stepped tectonics (green arrow) (Y3) during the 4 to 2.5 Ma; compound of long eccentricity and stepped tectonics (yellow) ($Y4 = Y2\times Y3$).

Figure 1.

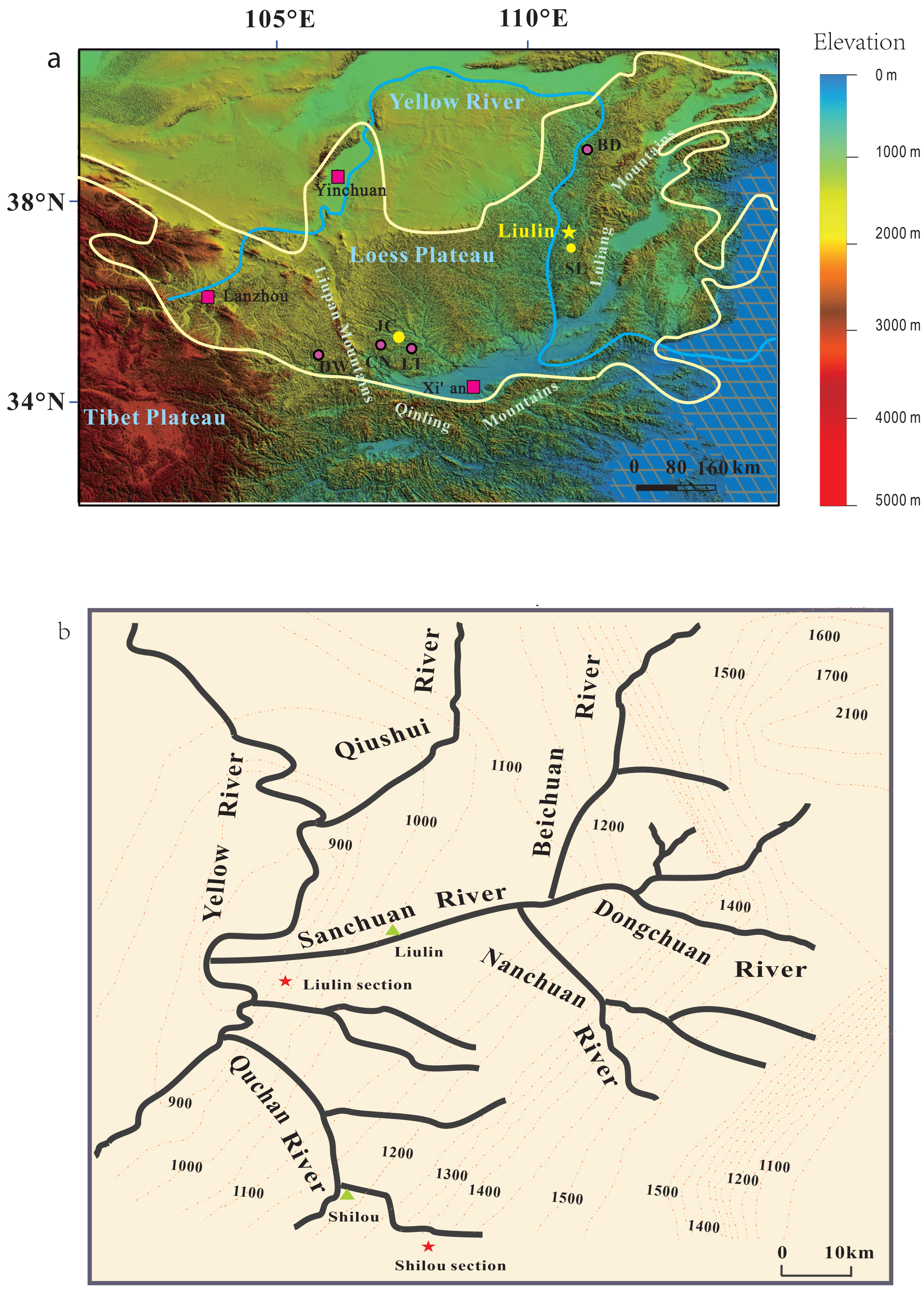
a
105°E
110°E
38°N
34°N
Elevation
0 m
1000 m
2000 m
3000 m
4000 m
5000 m
Yellow River
Loess Plateau
Tibet Plateau
Yinchuan
Lanzhou
Xi' an
Liulin
SL
BD
JC
CN
LT
DW
Liupan Mountains
Luliang Mountains
Qinling Mountains
0 80 160 km
b
Yellow River
Qiushui River
Beichuan River
Sanchuan River
Dongchuan River
Nanchuan River
Quchan River
Liulin
Liulin section
Shilou
Shilou section
0 10km

Figure 2.

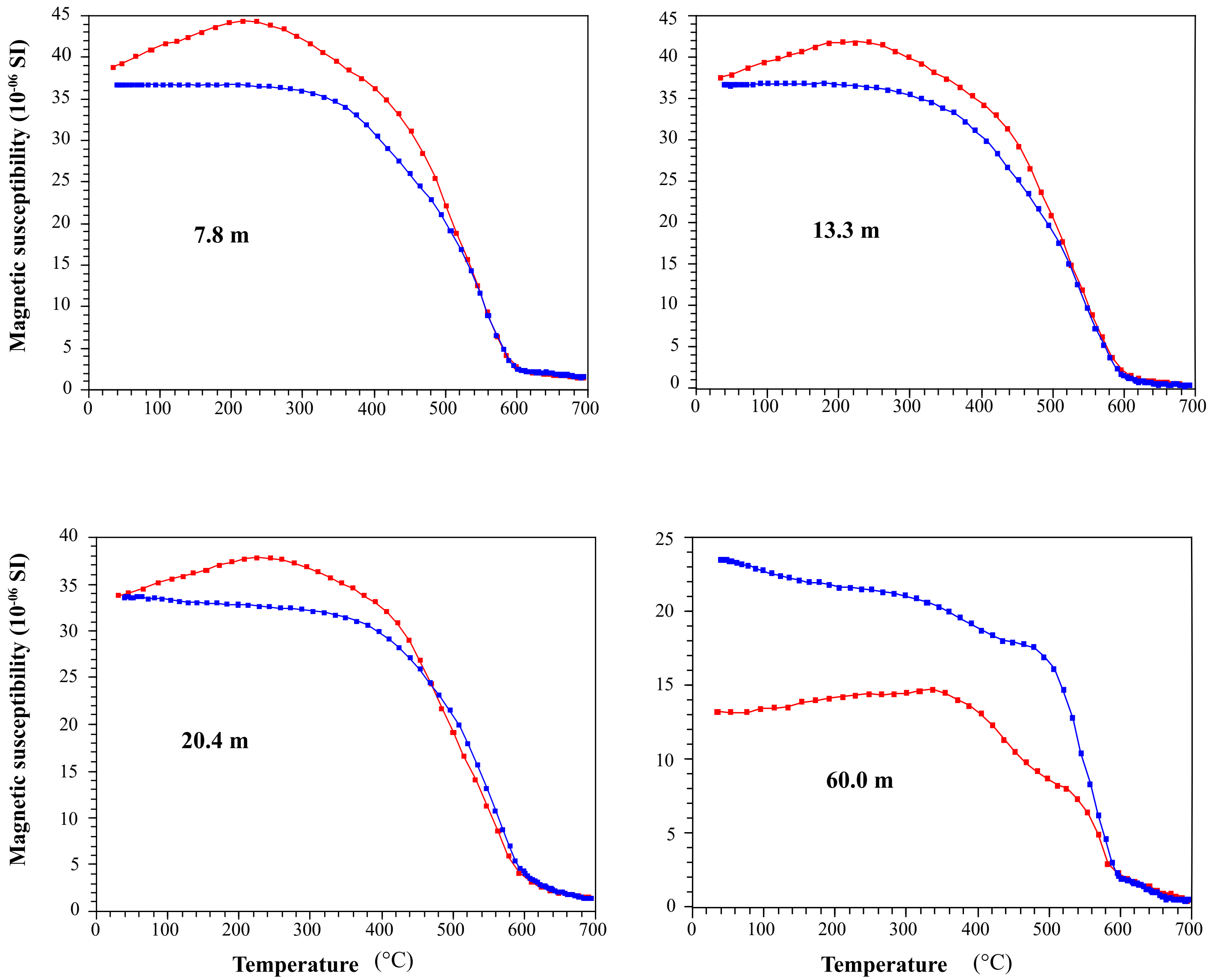
7.8 m
13.3 m
20.4 m
60.0 m
Magnetic susceptibility (10-06 SI)
Temperature (°C)

Figure 3.

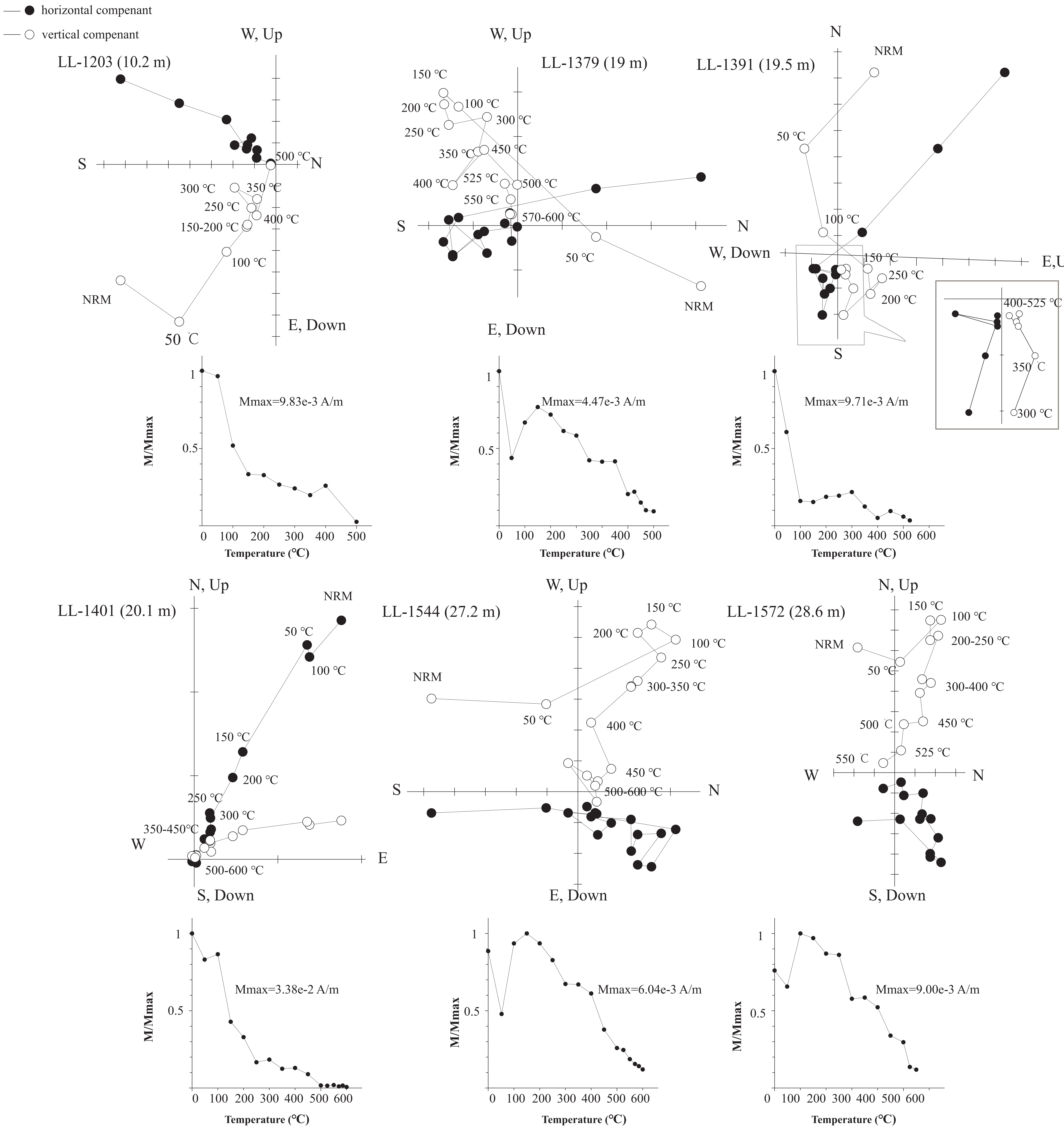

horizontal compenant
vertical compenant
LL-1203 (10.2 m)
W, Up
S
N
E, Down
500 °C
300 °C
350 °C
250 °C
400 °C
150-200 °C
100 °C
NRM
50 °C
Mmax=9.83e-3 A/m
M/Mmax
Temperature (°C)
LL-1379 (19 m)
W, Up
150 °C
200 °C
100 °C
300 °C
250 °C
350 °C
450 °C
400 °C
525 °C
500 °C
550 °C
570-600 °C
S
N
50 °C
NRM
E, Down
Mmax=4.47e-3 A/m
M/Mmax
Temperature (°C)
LL-1391 (19.5 m)
N
NRM
50 °C
100 °C
W, Down
E,Up
150 °C
250 °C
200 °C
S
400-525 °C
350 °C
300 °C
Mmax=9.71e-3 A/m
M/Mmax
Temperature (°C)
LL-1401 (20.1 m)
N, Up
NRM
50 °C
100 °C
150 °C
200 °C
250 °C
300 °C
350-450°C
W
E
500-600 °C
S, Down
Mmax=3.38e-2 A/m
M/Mmax
Temperature (°C)
LL-1544 (27.2 m)
W, Up
150 °C
200 °C
100 °C
250 °C
NRM
300-350 °C
50 °C
400 °C
450 °C
S
500-600 °C
N
E, Down
Mmax=6.04e-3 A/m
M/Mmax
Temperature (°C)
LL-1572 (28.6 m)
N, Up
150 °C
100 °C
200-250 °C
NRM
50 °C
300-400 °C
500 °C
450 °C
525 °C
550 °C
W
N
S, Down
Mmax=9.00e-3 A/m
M/Mmax
Temperature (°C)

Figure 4.

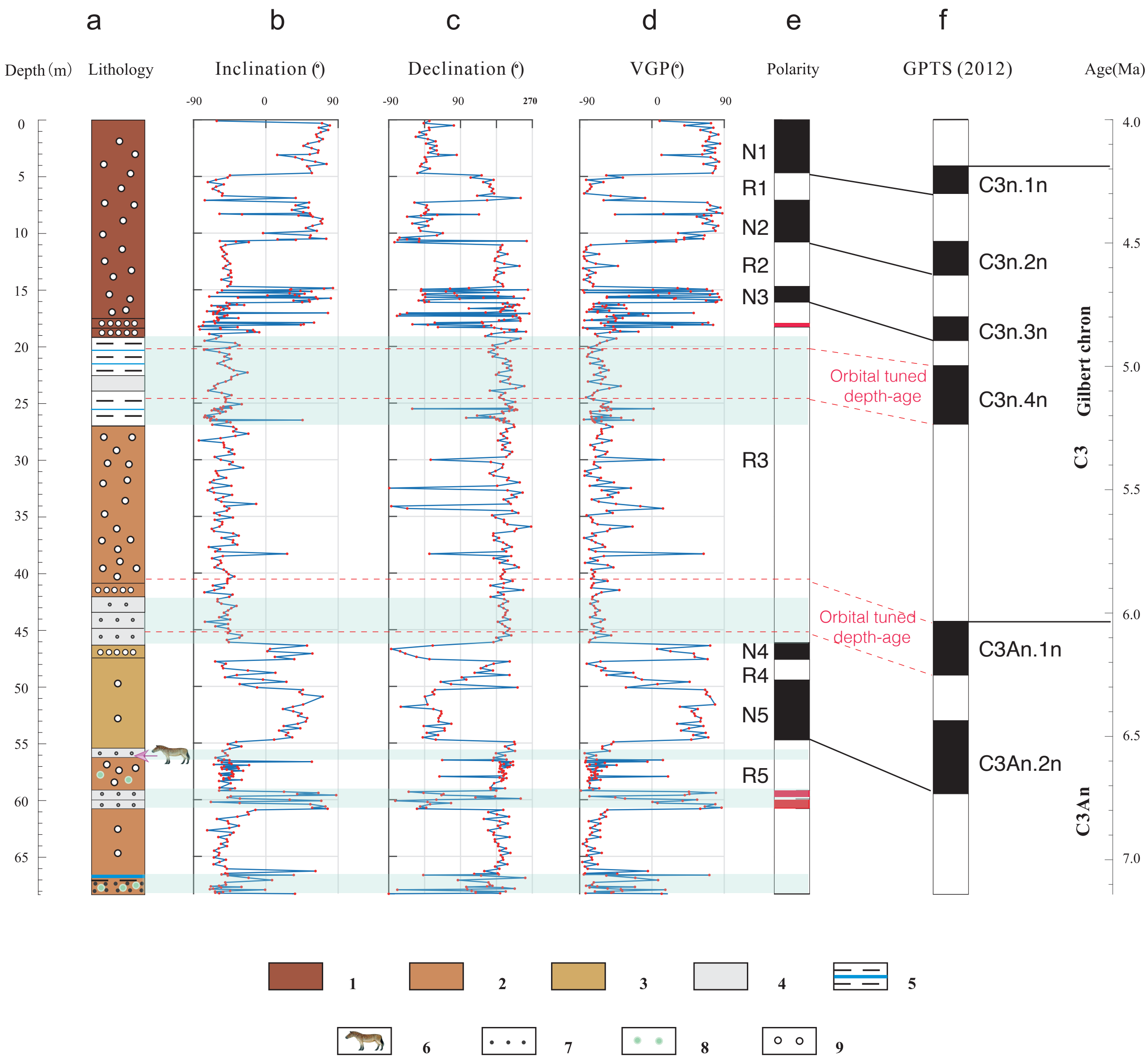
a
b
c
d
e
f
Depth (m)
Lithology
Inclination (°)
Declination (°)
VGP(°)
Polarity
GPTS (2012)
Age(Ma)
N1
R1
N2
R2
N3
R3
N4
R4
N5
R5
C3n.1n
C3n.2n
C3n.3n
C3n.4n
C3An.1n
C3An.2n
Orbital tuned depth-age
Orbital tuned depth-age
Gilbert chron
C3
C3An
1
2
3
4
5
6
7
8
9

Figure 5.

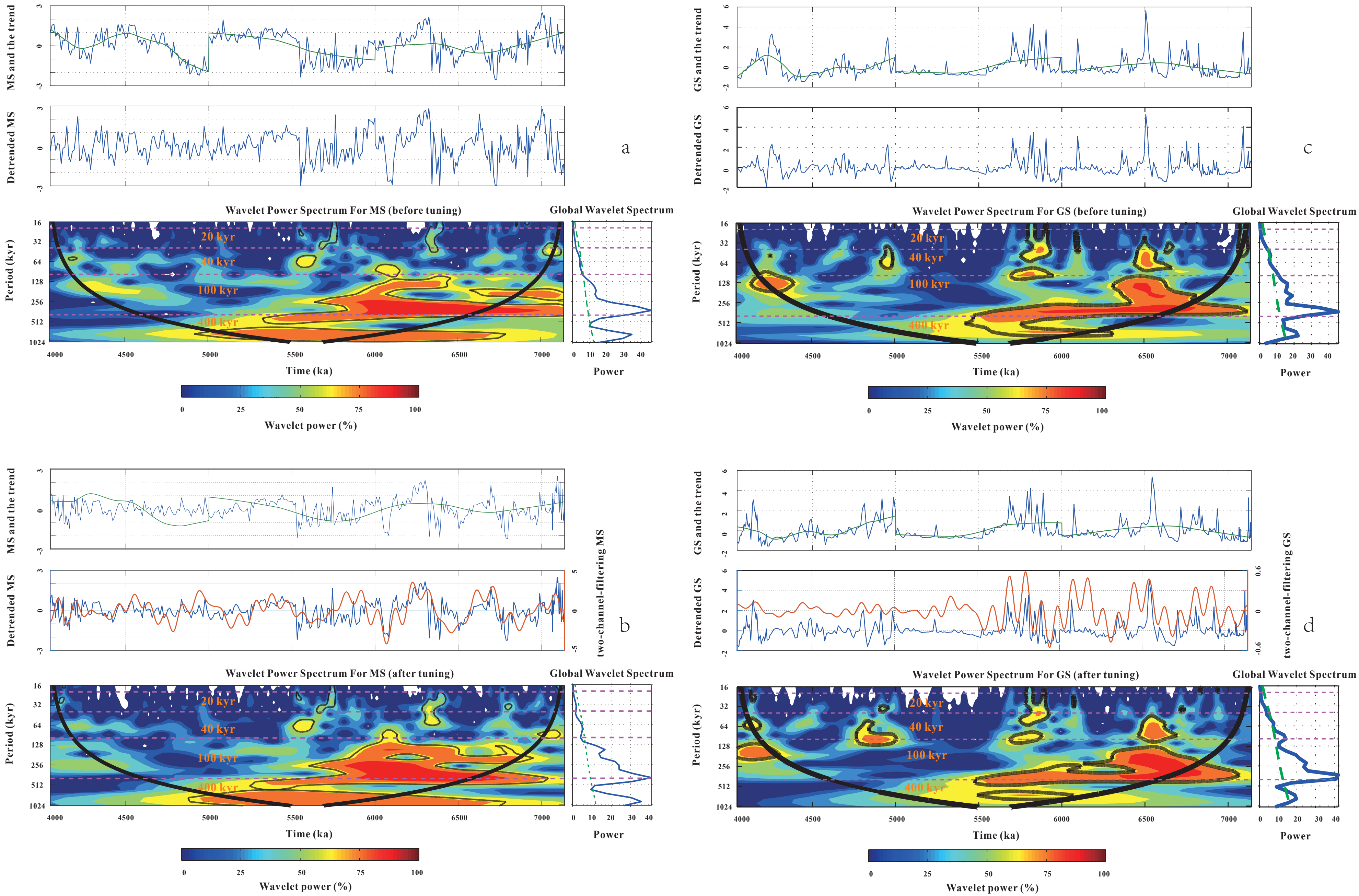
MS and the trend
Detrended MS
a
Wavelet Power Spectrum For MS (before tuning)
Global Wavelet Spectrum
Period (kyr)
20 kyr
40 kyr
100 kyr
400 kyr
Time (ka)
Power
Wavelet power (%)
GS and the trend
Detrended GS
c
Wavelet Power Spectrum For GS (before tuning)
b
two-channel-filtering MS
Wavelet Power Spectrum For MS (after tuning)
d
two-channel-filtering GS
Wavelet Power Spectrum For GS (after tuning)

Figure 6.

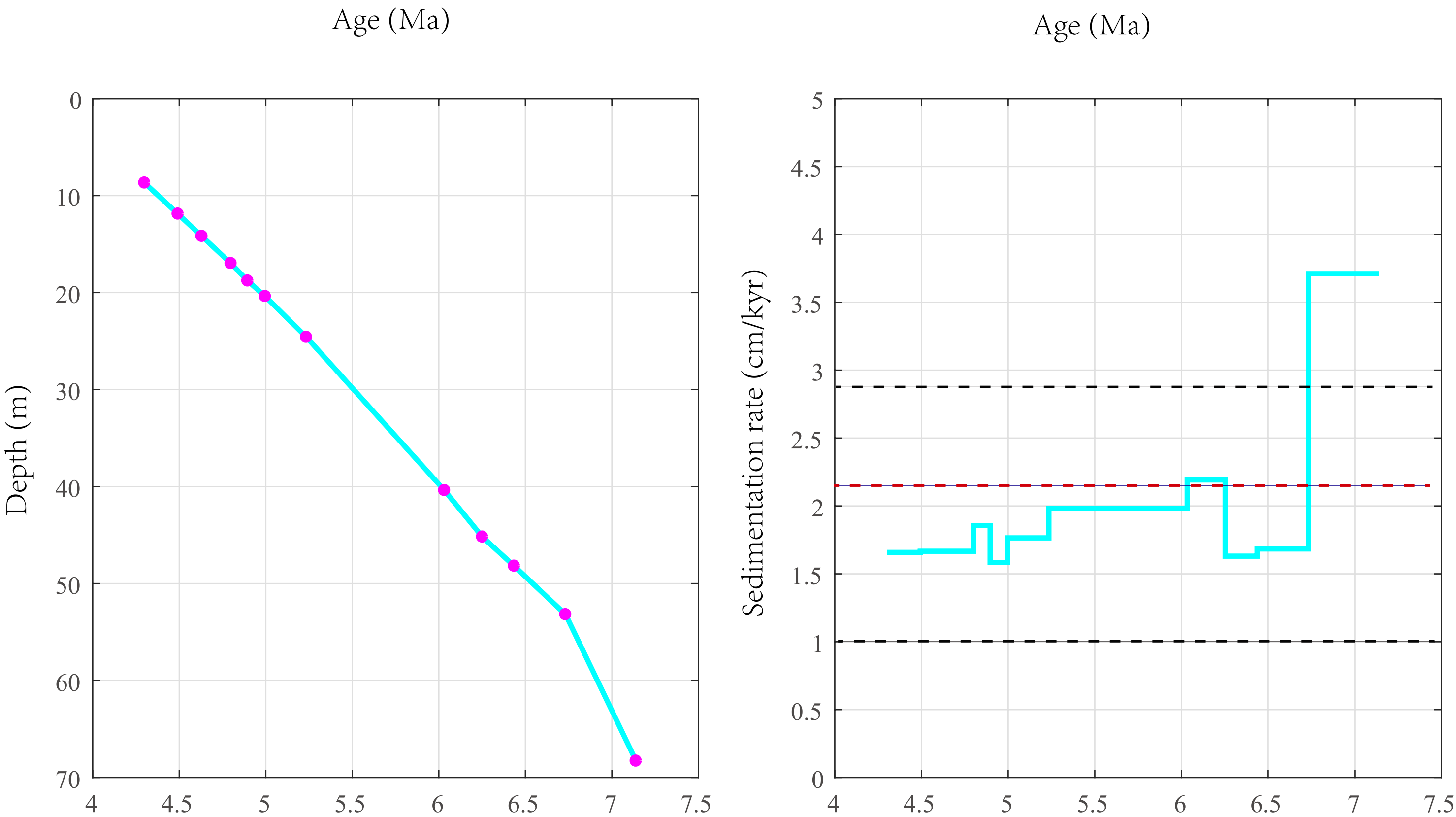

Age (Ma)
Depth (m)
0
10
20
30
40
50
60
70
4
4.5
5
5.5
6
6.5
7
7.5
Age (Ma)
Sedimentation rate (cm/kyr)
0
0.5
1
1.5
2
2.5
3
3.5
4
4.5
5
4
4.5
5
5.5
6
6.5
7
7.5

Figure 7.

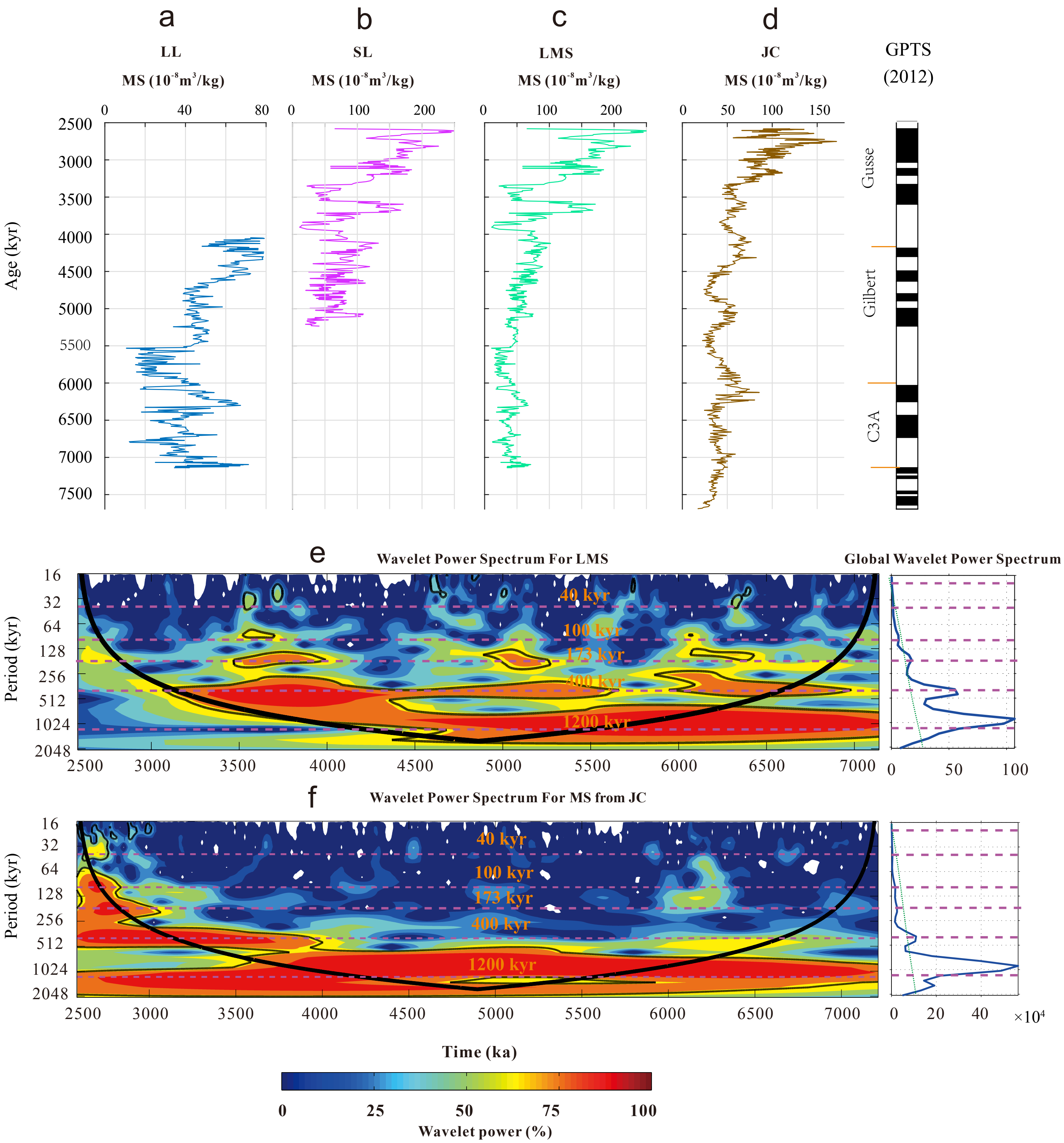

a
LL
MS (10-8m3/kg)
b
SL
MS (10-8m3/kg)
c
LMS
MS (10-8m3/kg)
d
JC
MS (10-8m3/kg)
GPTS
(2012)
Age (kyr)
Gusse
Gilbert
C3A
e
Wavelet Power Spectrum For LMS
Global Wavelet Power Spectrum
Period (kyr)
40 kyr
100 kyr
173 kyr
400 kyr
1200 kyr
f
Wavelet Power Spectrum For MS from JC
×10^4
Time (ka)
Wavelet power (%)

Figure 8.

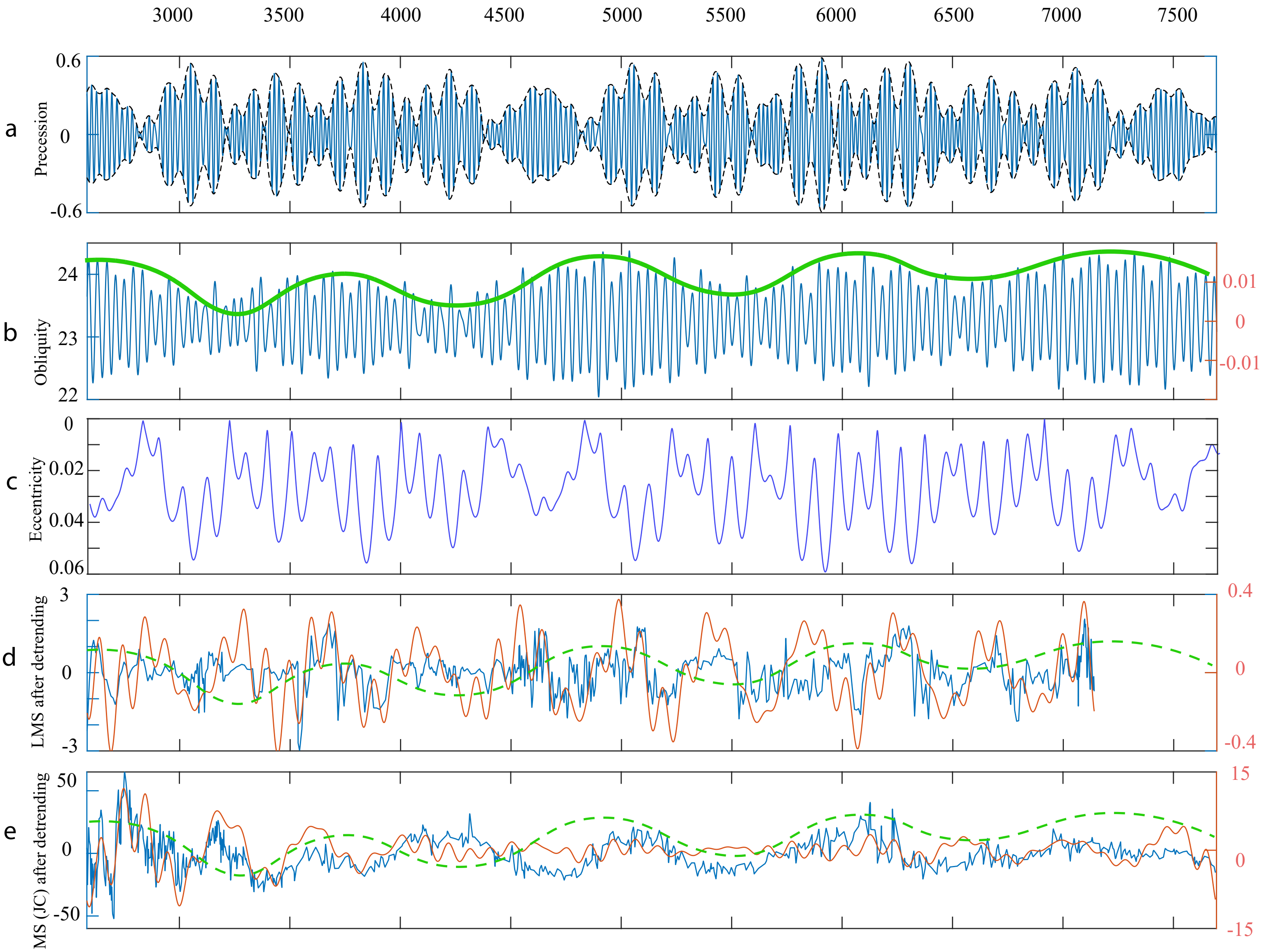

3000
3500
4000
4500
5000
5500
6000
6500
7000
7500
a
Precession
0.6
0
-0.6
b
Obliquity
24
23
22
0.01
0
-0.01
c
Eccentricity
0
0.02
0.04
0.06
d
LMS after detrending
3
0
-3
0.4
0
-0.4
e
MS (JC) after detrending
50
0
-50
15
0
-15

Figure 9.

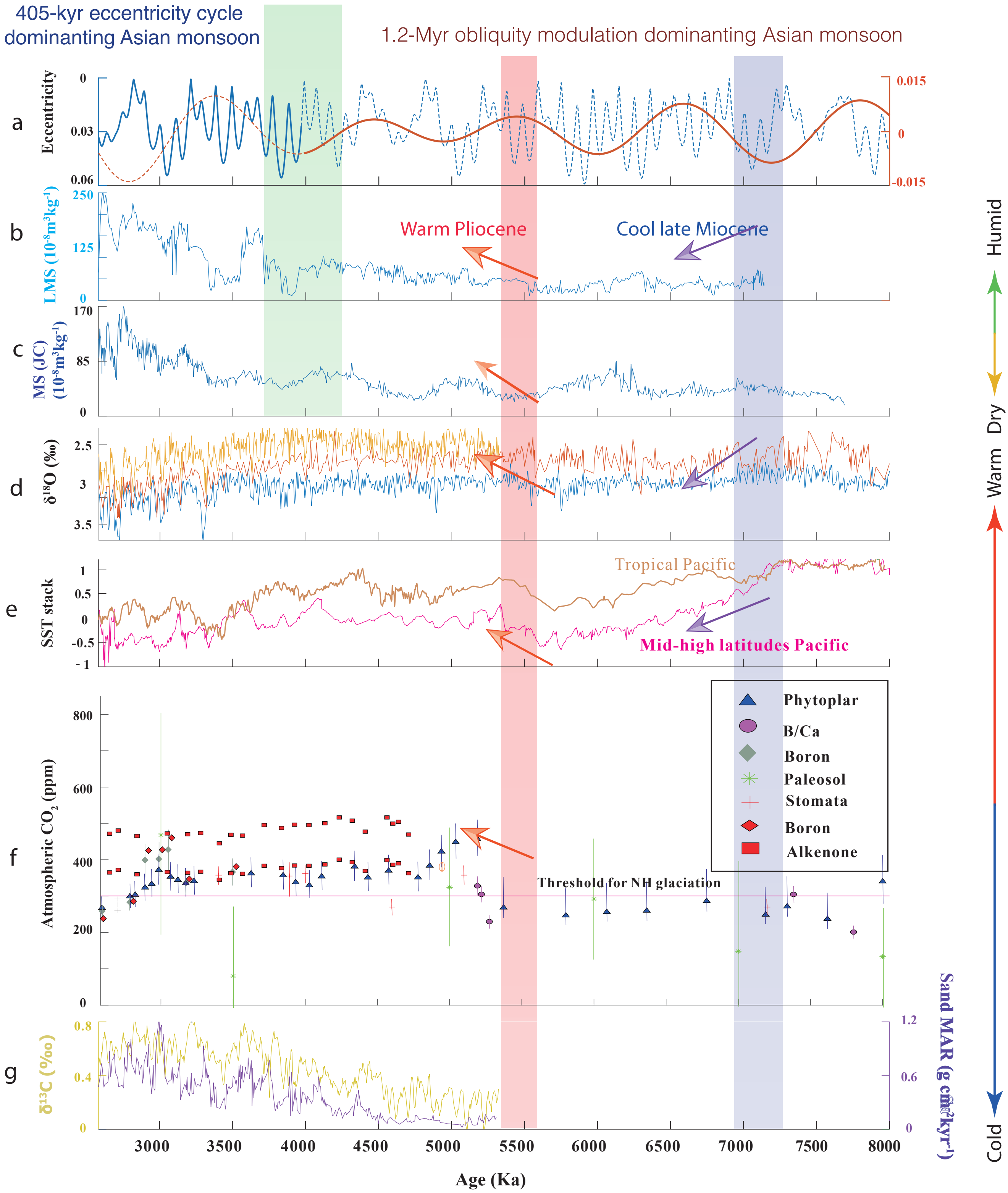

405-kyr eccentricity cycle dominanting Asian monsoon
1.2-Myr obliquity modulation dominanting Asian monsoon
a
Eccentricity
0
0.03
0.06
0.015
0
-0.015
b
LMS (10-8m3kg-1)
250
125
0
Warm Pliocene
Cool late Miocene
c
MS (JC) (10-8m3kg-1)
170
85
0
d
δ18O (‰)
2.5
3
3.5
e
SST stack
1
0.5
0
-0.5
-1
Tropical Pacific
Mid-high latitudes Pacific
f
Atmospheric CO2 (ppm)
800
600
400
200
0
Threshold for NH glaciation
Phytoplar
B/Ca
Boron
Paleosol
Stomata
Boron
Alkenone
g
δ13C (‰)
0.8
0.4
0
Sand MAR (g cm-2kyr-1)
1.2
0.6
0
3000
3500
4000
4500
5000
5500
6000
6500
7000
7500
8000
Age (Ka)
Humid
Dry
Warm
Cold

Figure 10.

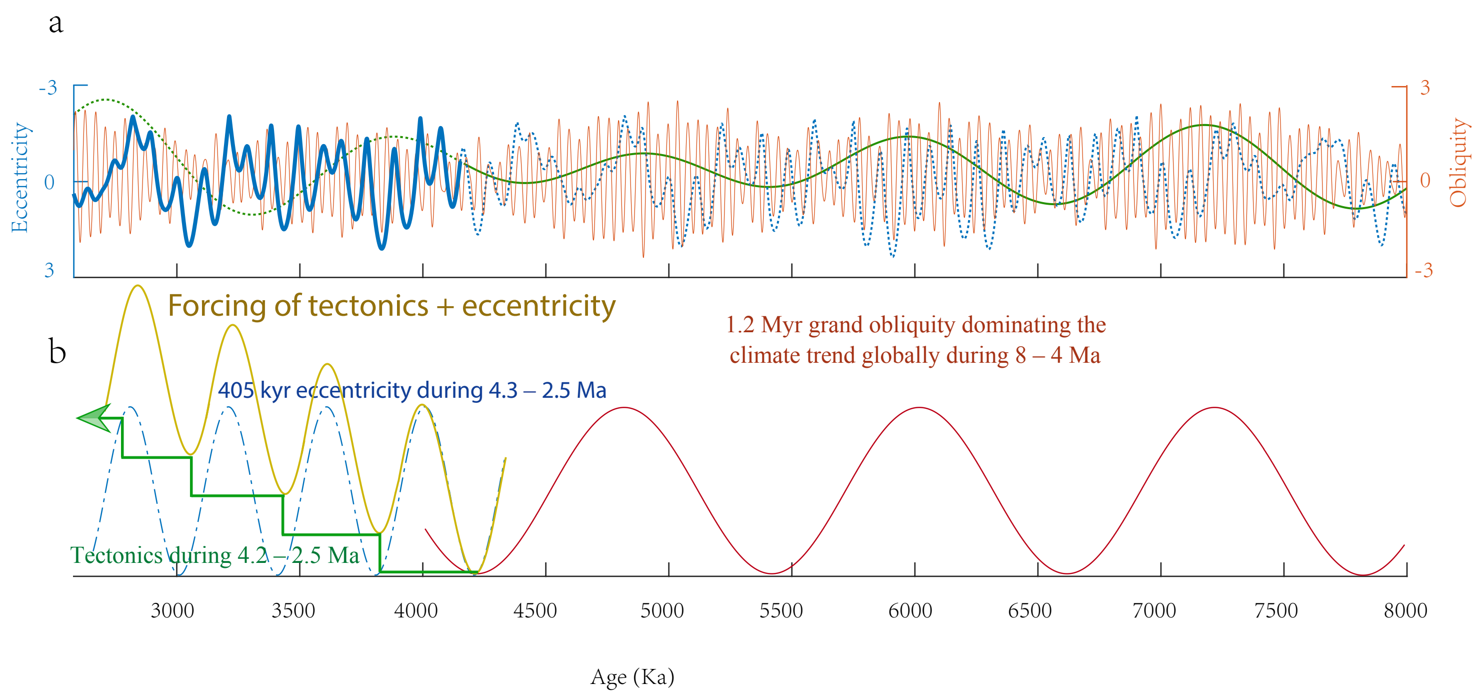
a
b
Eccentricity
-3
0
3
Obliquity
3
0
-3
Forcing of tectonics + eccentricity
1.2 Myr grand obliquity dominating the
climate trend globally during 8 – 4 Ma
405 kyr eccentricity during 4.3 – 2.5 Ma
Tectonics during 4.2 – 2.5 Ma
3000
3500
4000
4500
5000
5500
6000
6500
7000
7500
8000
Age (Ka)